Chapter 1

Appendix A

1.1 PCB design

1.1.1 Choice of components

Optocoupler

A dual optocoupler (HCPL-263A-000E, RS) operating over an appropriate range and with consistent rise and fall times was chosen to isolate the Arduino from the high-power circuit. The selected optocoupler functions in inverting logic: the signal is transmitted if the input diode is off. Considering the specifications of the input diodes, I chose to positively bias the diode's cathode at +5 V and to connect the Arduino output to the anode such as a high signal from the Arduino resulted in +5 V on the anode, shutting the diode off. A resistor network was connected to the diodes' terminals to limit input currents and to ensure the negative biasing of the diode in the "on" phase, guaranteeing the activation of the optocoupler. The +5 V bias was regulated through a low-dropout voltage regulator (TLC317, RS) to ensure a precise, steady +5 V supply. The output of the optocoupler used a +5 V reference voltage supply which was also regulated by a low-dropout voltage regulator in a similar setup as on the input, and a set of pull-up resistors between the outputs and the +5 V rail, which were chosen as recommended by the manufacturer.

CMOS level-shifter

A supplementary stage of isolation was implemented through a CMOS level-shifter (DG445B, Vishay), which also ensured stable voltage levels to drive the BJT transistors' gates. The voltage supply as well as the voltage level (set as +5 V as well) were both provided by different LDO regulators in similar arrangements as described before. Two out of four channels were used, and the outputs were connected to the trigger transistor's gate (through the 5 kΩ potentiometer) and the delay transistor's gate (through an RC filter).

1.1.2 Circuit prototyping

The whole circuit prototype was tested on a breadboard with a resistor as load in place of the electrodes. The transmission of the control signals was evaluated through each isolation stages in terms of amplitude and timing, and the stimulation waveform was characterised at the resistive load for different cathodic currents. After prototyping validation, components were assembled on the PCB first, then wires for the +30 V supply, electrode wires, and 4mm wire terminals were added, and the circuit was characterised again. Timings, amplitudes and compliance were consistent with the prototyping tests, however, a few adjustments were made to improve the waveform. First, ripples were observed in the cathodic square wave (Fig. 1.1 B), which were attributed to some resonance in the circuit. The hypothesis of resonance was confirmed by delivering pulses with longer pulse width which showed the ripples amplitude decreased over time (Fig. 1.1 C). The period of the oscillations was recorded and two capacitors were placed between both Arduino signals and ground. Ripples were greatly reduced by the addition of capacitors without any visible secondary effect. Then, compliance of the circuit was evaluated for each cathodic current to be used in experiments (between 8.5 and 44.3 mA) by increasing the load between 50 Ω and 20 kΩ, which was sufficient to see saturation for all currents (Fig. 1.1). The current magnitude was set in the absence of load, and was not changed while the load was increased. The saturation manifested as the current source was not able to provide the set current value. The load at which the current source saturated decreased with increased current, as expected as higher currents generate higher ohmic drops across the circuit. The saturated current exhibited an exponential trend, which I modelled following Ohm's law to determine the true available voltage at the current source (Fig. 1.2).

Finally, pull-down resistors were added on the Arduino output channels to improve the pulses triggering. The "Single" trigger mode on the oscilloscope is used to record the first pulse out of the 1000 pulses train, and the trigger lead is connected to the trigger control signal. I noticed that in some cases, the oscilloscope was triggered before the first pulse, which was thus missed, despite actively commanding the pin to stay at a low value ($= 0$ V). After investigation, it was attributed to the functioning of Arduino, which sets output pins to a high-impedance state. In that high-impedance state, the voltage is not controlled by the micro-controller as it is left floating, which would typically sit at around 2.5 - 3.5 V, which exceeded the trigger threshold. By adding a small (470 Ω) pull-down resistors on both output pins, the high-impedance state voltage was drastically reduced (< 1 V), while the high voltage state was only slightly lower (between 4.5 V and 5 V), which are both far away from the trigger threshold set at 2.52 V.

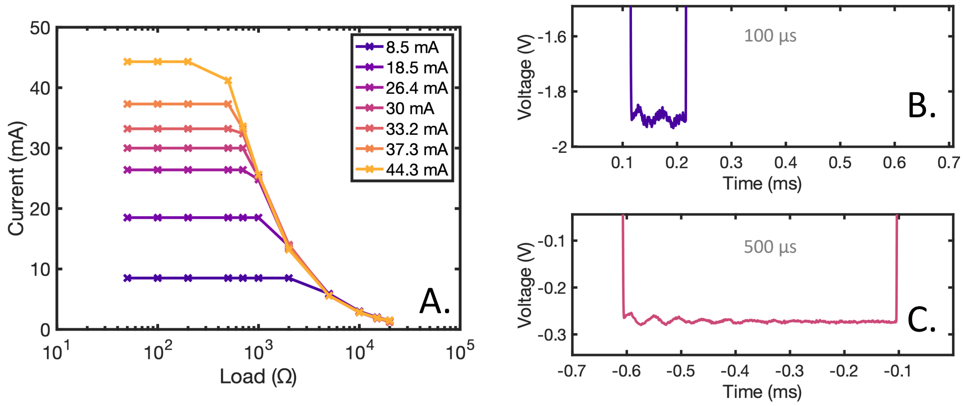

Figure 1.1: *A. Compliance criteria: if the stimulation current at the end of the cathodic phase was less than 90% of the starting value, the circuit was considered to saturate. B. Compliance testing on various resistive loads. C. Observed ripples with a) 100µs and b) 1 ms pulse widths.*

Circuit characterisation: charge balance

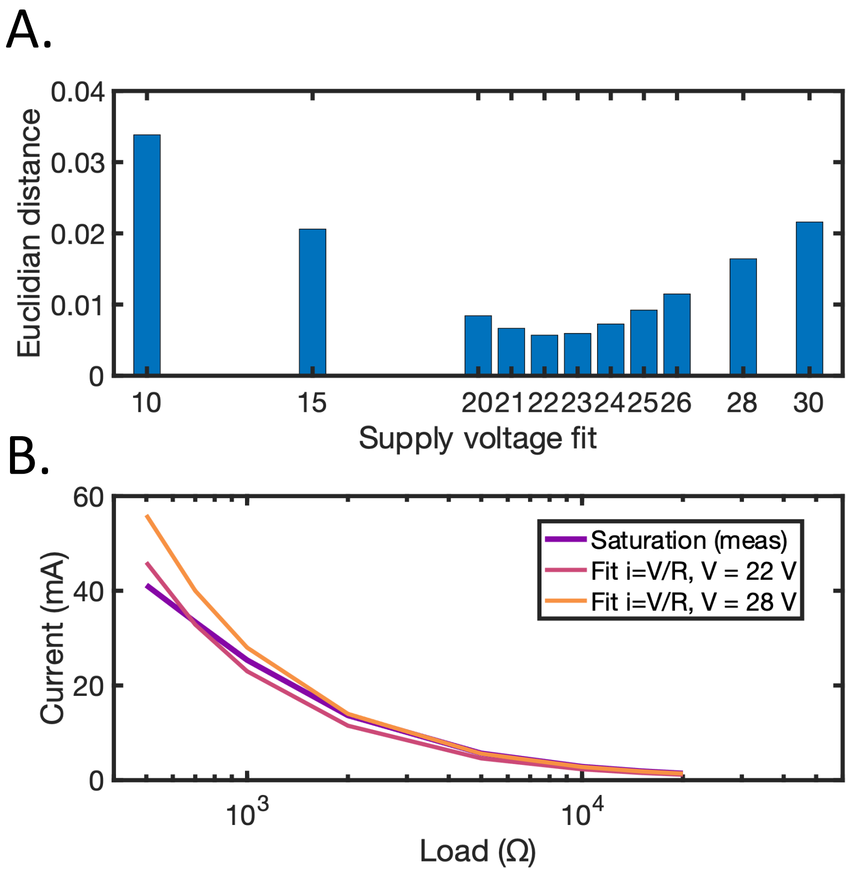

Figure 1.2: *Estimation of the compliance voltage from saturation current fitting. The top graph shows the cumulated error (Euclidian distance) for various supply voltages and the bottom graph shows the fits for the lowest cumulated error (22 V) and the closest curve match (28 V).*

Charge balance was a key characteristic of the stimulator as charge-balanced pulses were used in the studies on which Shannon's limit was based, and on subsequent studies studying Shannon's limit [Kumsa et al., 2016, 2017]. Thus, charge balance was assessed with a range of methods. Originally, charge balance was asserted through the full discharge of the capacitor, demonstrating that 100% of the charge accumulated during the cathodic phase was injected back in the anodic phase. As mentioned previously, the current waveform did return to null current well within the discharge period, so there was no doubt that the discharge could be completed within the 19.8 ms delay, and so did the capacitor voltage, demonstrating that no charge remained stored in the capacitor. Indeed, to determine whether high impedances may challenge the capacitor's ability to discharge, the current waveform was tested for various resistive loads in place of the electrodes. The circuit's time constant $\tau = \frac{1}{R_{load}Cdis}$ was calculated and the theoretical discharge timings for 50% (=$ln(2)\tau$) and 90% (=3τ) were compared with experimental timings. Experimental timings increased linearly with the load as expected, showing good agreement with the theory, although remaining consistently slightly lower. Therefore, it was estimated from the theoretical time constant that for loads up to 4 kΩ, the discharge was completed at 99% within 19.8 ms, and for superior loads, the discharge time would need to be increased.

Then, charge balance was quantified by estimating the cumulative injected charge during pulses: a short programming bit was written in the analysis Matlab code to estimate the net injected charge in the pulse by integrating the current waveform versus time for the 1000^{th} pulse. A trapezoidal estimation function was used (”trapz” function) to quantify separately the cathodic and anodic charge, and a the cumulative charge was calculated and plotted using the ”cumtrapz” function of which an example is showed in figure **??** B). Several estimates were considered to calculate the real injected charge. For the cathodic charge, considering rise and fall times, and current fluctuation, trapezoidal estimates of the raw current waveform including and excluding rise times were compared to a raw estimate of mean current x pulse width and the results were similar with less than 3.5% discrepancy between extreme cases. For the anodic charge, a trapezoidal estimate of the raw current was compared with an integral of an exponential fit of the data with 99% discharge and to infinity, with results fluctuating by less than 3%. Despite these consistent estimates, the cumulative charge plot exhibited a lot of fluctuations from one test to another with final net charge estimate fluctuating between +0.5 μC and -0.5 μC with rare spikes larger than ± 1 μC. The fluctuation were attributed to noise and an inaccurate estimation of the base current (average current meaasured in the null current region before the pulse) which led to an incorrect integral estimation. Especially, although the imbalance was mostly negative ($Q_{cat} > Q_{ano}$,

$\approx$ 70% of the time), the frequent positive imbalance suggesting more charge was injected in the anodic appeared as an inaccurate estimation, which led me to think that the charge balance was correct, following the capacitor discharge characterisation, but the estimation was inaccurate.

The interphase voltage loss increased with k from 27 mV to 53 mV, representing a charge loss of 1.13 ± 0.12% of the injected charge, which did not increase with k. However, the recorded values exhibited some volatility and no clear trend, similarly to the charge balance characterisation, which may also suggest that the voltage loss may be a measurement artifact. Indeed, the charge loss measurements during the interphase are not conclusive as the differential probe's time constant $\tau_{DP} = 4\,M\Omega\,5.5pF = 22\mu s$ was of the same order of magnitude as the interphase delay. Especially the voltage loss had an exponential shape, with most of the voltage decrease happening in the first μs after the end of the cathodic phase, which could correspond to the differential probe measurement accuracy settlement.

1.2 Data analysis script

Several steps were needed to accurately estimate the ohmic drop. First, the start and end of the cathodic and anodic phases were identified using a peak finding algorithm (”findpeaks”) on the differential vector (subtraction of neighbour values) of the waveforms, which provided peak index and peak widths, which quantified the rise and fall times (Fig. 3.5 A). Incorrect estimation of the access voltage may be the source of significant errors [Harris, 2024], and internal hardware limitations make it difficult to estimate the "instantaneous" voltage drop when it occurs over several timepoints. Several estimates of the access voltage (shown in figure 3.5 C) were compared using the peak widths and the most robust method was selected: the voltage before and after each peak was averaged over 50 timepoints (5 μs) and the difference was calculated as the access voltage, the same thing was done with the current, and the access resistance was obtained by dividing voltage by current. Although the voltage

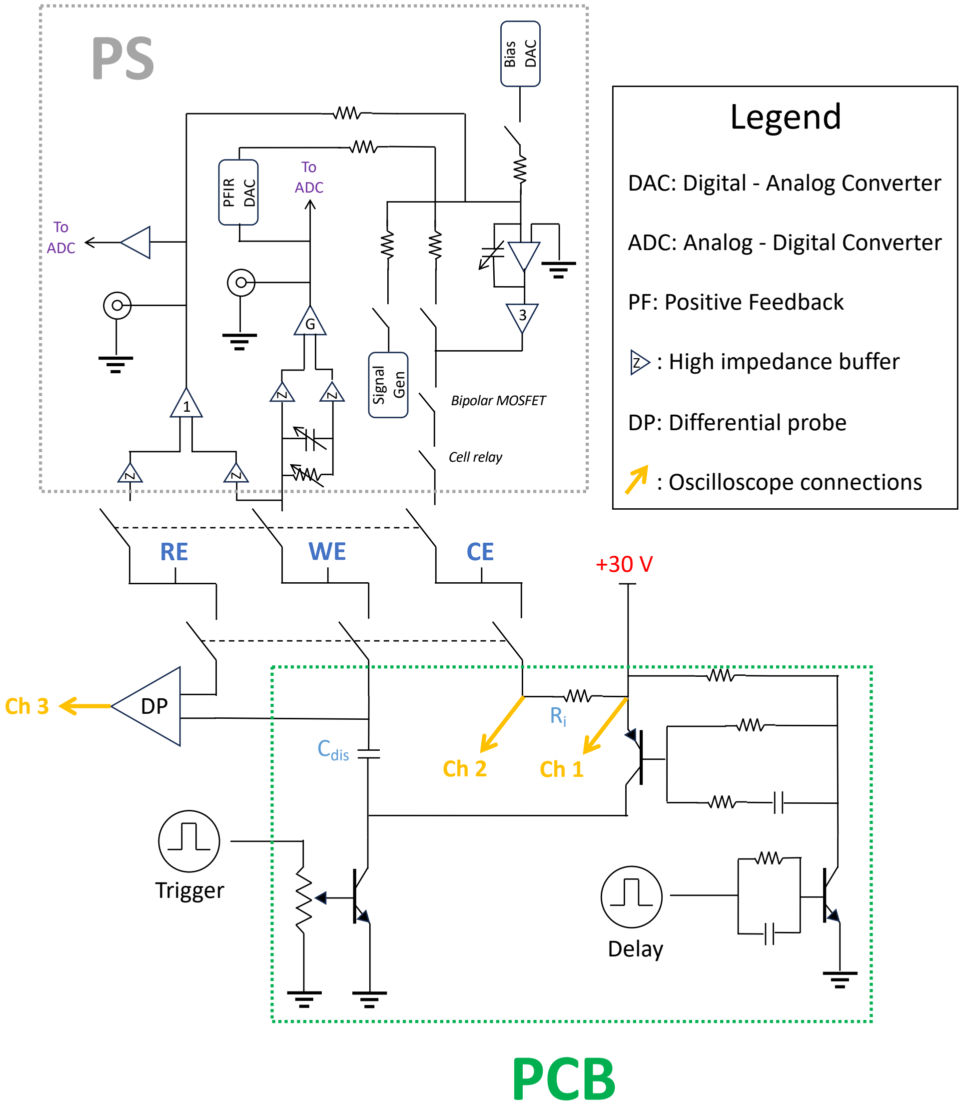

Figure 1.3: *Schematic of the experimental setup detailing the connections to the different measuring devices. PS is the potentiostat (circuit diagram found in manufacturer's resources), PCB is the custom made stimulator.*

drops were different at each peak [**?**], the calculated access resistance was consistent with 2.1% discrepancy and matching the high frequency impedance measured in EIS. The averaging approach allowed us to avoid overestimating the access voltage due to noise or switching artifacts and to have a robust automatic method of detecting the ohmic drop despite internal hardware limitations. A few manual adjustments were still required to produce the plots due to possible misalignments between current and voltage waveforms (usually less than 0.5 μs) and a few artificial spikes remained on the polarisation plots due to the non-instantaneous ohmic drop (Fig. 3.5 D).

1.3 Circuit modifications to avoid the passive decay during pulses

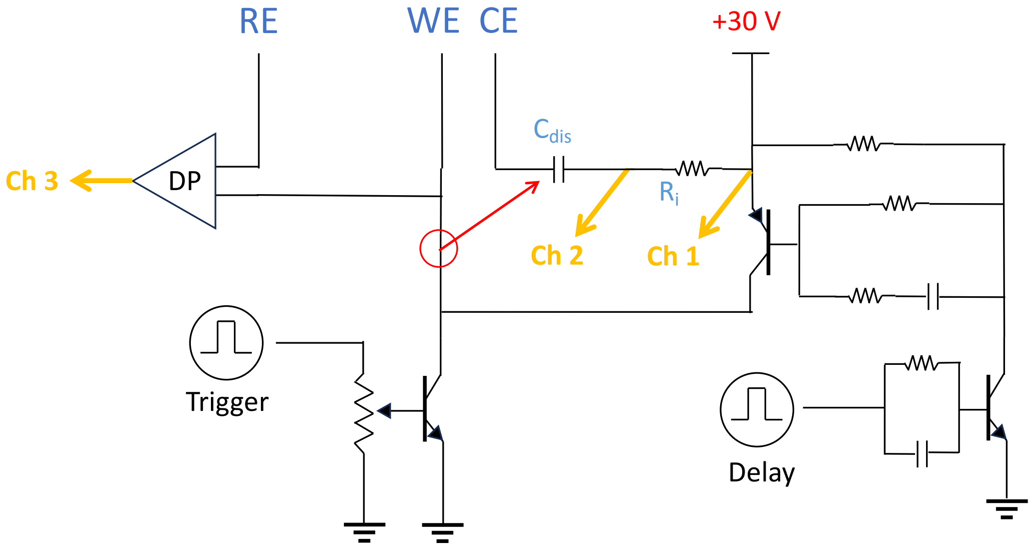

Figure 1.4: *Schematic of the alternative circuit architecture to stop leaking current from flowing. The discharge capacitor was moved closer to the power supply, the initial capacitor position is indicated by a red circle.*

The potential decay due to the +30 V supply was studied in detail so it could be eliminated. According to Bard et al. [2022], the observed potential waveform when the +30V supply was turned on corresponds to low current chronopotentiometry, meaning a low current was able to flow between the

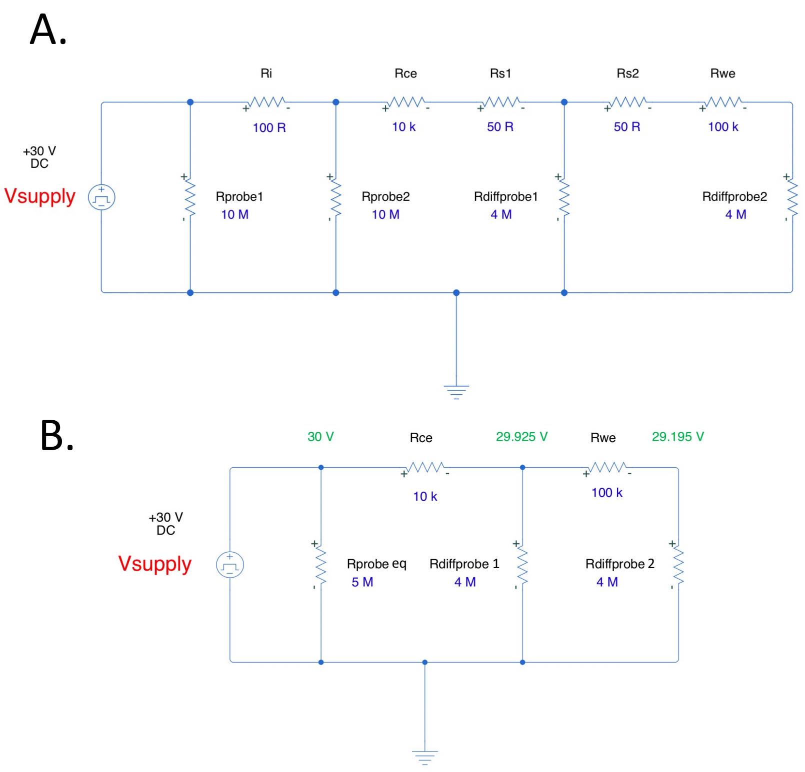

Figure 1.5: *A. Schematic of the Thevenin approximation of the current flow loop to estimate the leakage current magnitude and compare with decay measurements. B. Simplified Thevenin circuit.*

electrodes even when the circuit was supposed to be open. We attributed this small current flow to leakage through the measurement apparatus (either oscilloscope probes (10 MΩ) or differential probe (4 MΩ)), which represented the lowest impedance path (Fig. 1.4). The magnitude of a such current was calculated using a Thevenin equivalent circuit with estimated impedances along the current path: the electrodes were approximated using Randle's model (see section 1.2.2), and considering DC conditions, the capacitors are equivalent to open switches. The DC resistance values were then estimated, with R_{WE} estimated as the impedance module recorded at the lowest frequency in EIS scans ($R_{WE} \approx 100\,k\Omega$) and $R_{CE} \approx \frac{R_{WE}}{10}$. After a Thevenin circuit simplification, the Thevenin voltage was estimated in a voltage divider as $V_{Th} = \frac{4.10^6}{4.01.10^6}30 = 29.925\,V$, and with $R_{Th} \approx 4\,M\Omega$, $I_{No} = \frac{29.925}{4.10^6} \approx 7.48\,\mu A$, which matched with the hypothesis from Bard et al. [2022], which was valid for currents $\leq 10\ \mu A$.

To confirm the hypothesis and theoretical calculation, I referred to small current chronopotentiometry analysis by Bard et al. [2022] (Fig. 1.6 C.), which showed a similar shape as the observed potential decay, such as figure 1.6 A. Bard et al. [2022] gives equations that model the potential change in the case of a fully reversible reaction (Nernstian, Eq 1.1) and fully irreversible reaction (Tafelian, Eq 1.2).

$$E = E^{0'} + \frac{RT}{2nF} ln(\frac{D_O}{D_R}) + \frac{RT}{nF} ln(\frac{\tau^{1/2} - t^{1/2}}{t^{1/2}}) \tag{1.1}$$

$$\text{with} \quad E_{\tau/4} = E^{0'} + \frac{RT}{2nF} ln(\frac{D_O}{D_R})$$

$$E = E^{0'} + \frac{RT}{2\alpha F} ln[\frac{2k^0}{(\pi D_O)^{1/2}}] + \frac{RT}{\alpha F} ln(\tau^{1/2} - t^{1/2}) \tag{1.2}$$

$E^{0'}$ is the equilibrium potential, D_O and D_R are the respective diffusion coefficients of oxidant and reductor, and k^0 the rate constant for the electrode reaction (see equation 1.6). A simple condition is also provided to determine whether reversible or irreversible reactions support the small current injection: with τ the typical time between two vertical asymptotes in the potential decay, if the potential trace between $E_{\tau/4}$ and $E_{3\tau/4}$ can be approximated linearly, the reaction is reversible if $\mid E_{\tau/4} - E_{3\tau/4} \mid = \frac{0.0479}{n}$, with n number of electrons exchanged and irreversible if $\mid E_{\tau/4} - E_{3\tau/4} \mid = \frac{0.0338}{\alpha}$, with α the charge transfer coefficient (see **??**). The linear fits of $\mid E_{\tau/4} - E_{3\tau/4} \mid$ in two cases are presented in figure 1.6; the decay were well aproximated by a linear fit, however, the slope did not match either case put forward by Bard et al. [2022] with respectively 1.2 mV/s for A. and 0.8 mV/s for B., which would correspond to the unlikely event of high numbers of electrons exchanged. The lower potential decay rates compared to rates expected in Bard et al. [2022] may suggest a kinetically slow process, however, despite the match in potential trace shape (especially for figure 1.6 A.), the exact electrochemical mechanism remained unknown. Nonetheless, the linear fits showed that the decay remained limited as the pulse tests lasted for 20 s, generating a potential change of 24 mV for

A. and 16 mV for B.

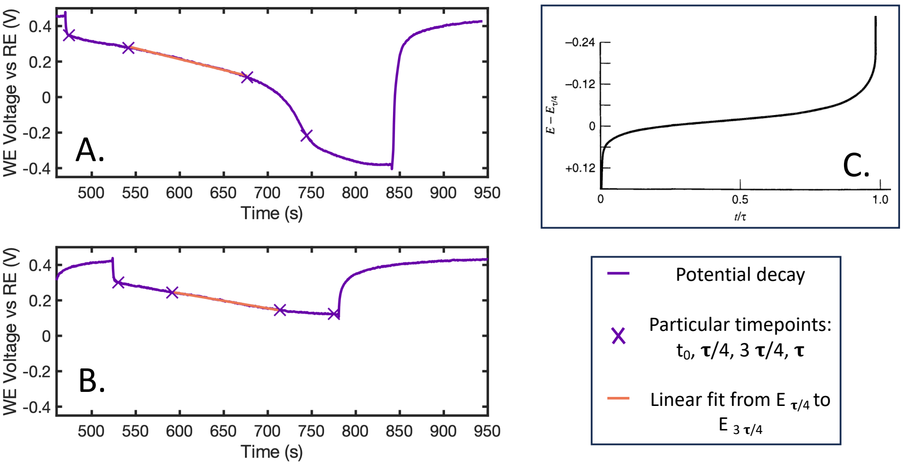

Figure 1.6: *Fit of potential decays according to Bard et al. [2022] in two electrolytes: A. NaCl gel electrolyte, B. NaCl solution.*

To hinder current flow, several options were explored. Ideally, a physical switch closing simultaneously with the first pulse would guarantee no current flow before pulses start. However, other problems may have appeared, such as imperfect synchronisation of pulses and switch, and the modifications of the existing circuit would have been substantial and we decided not to take this risk. Instead, it was decided to move the capacitor higher in the power line, between the current measurement resistor and the CE (Fig. 1.4. This option allows to cut off the current flow before reaching the low impedance path by using a component that was already present in the circuit. The repositioning of the capacitor resulted in a lower ohmic drop and a negligible decay, which confirmed the current leak hypothesis and validated the new architecture (Fig. 1.7 A.).

However, the potentials recorded during pulsing were much higher than previous measurements, especially for E_{ano} and E_{end}, which were measured around +1.2V vs Ag|AgCl, independently of solution pH and of k (Fig. 1.7 B and C). These values arose suspicion as E_{ano} and E_{end} values corresponded to the potential of O-evolution and oxidation of water, one of the boundaries of the water window, which is to be avoided. Such high boundaries reached even

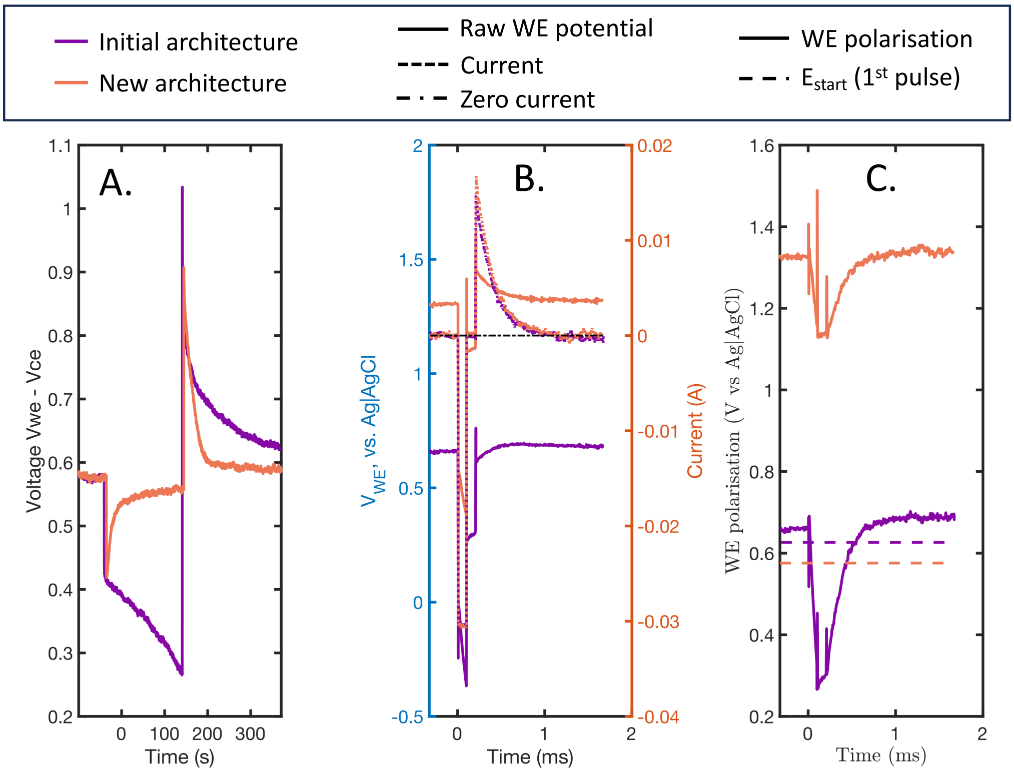

Figure 1.7: *A. Potential difference between WE and CE representing the current flowing between the electrodes while no pulses are applied. B.* 1000*th* *pulse potential and current waveforms for both circuit architectures. C. Polarisations calculated by removing the ohmic drop for B and starting potentials (first potential value of the first pulse).*

for low stimulation rates (for k as low as 0.566) suggested that there was a problem with the measurement setup. Indeed during the first pulse, the potential suddenly increased by several hundreds of mV during the first anodic discharge, which was much larger than in previous pulsing experiments and in subsequent pulses (Fig 1.8 B.). Tests showed that the capacitor was charging before the pulses started when the +30V supply was on and discharged during the first anodic discharge, which created a disproportionate discharge (11.9 μC injected in the anodic charge vs 2.9 μC in the cathodic charge, Fig. 1.8 A.), driving the potential more positive (+ 280 mV in the first pulse). Several adjustments were tested to mitigate this large discharge and potential step, but it remained unavoidable due to the circuit architecture. It was decided that the new position of the capacitor, even though it dampened the potential decay, was not making measurements more accurate and rendered the pulsing experiments irrelevant, since all potentials recorded were almost equal. The argument of precise charge-balance offered by the series capacitor was also deeply challenged in the new architecture, as one could clearly see how the first discharge amplitude greatly exceeded subsequent anodic discharges. The circuit architecture was then reverted to the previous version, which limitations were accounted for.

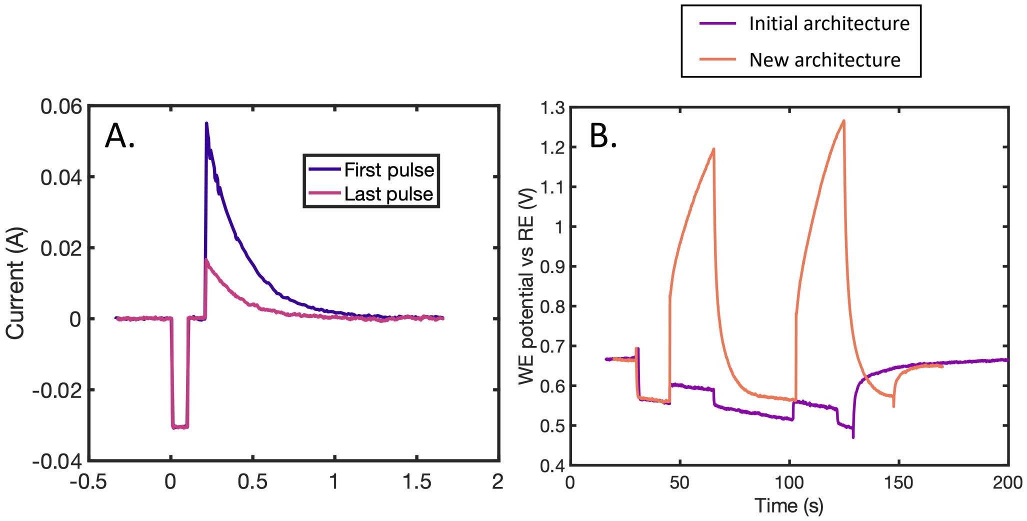

Figure 1.8: *A. Difference between the first and the last current pulse with the new circuit architecture. B. Comparison of WE potential decays during pulses for each circuit architecture (2 pulse trains).*

Chapter 2

Appendix B

2.1 Additional figures related to solution effect

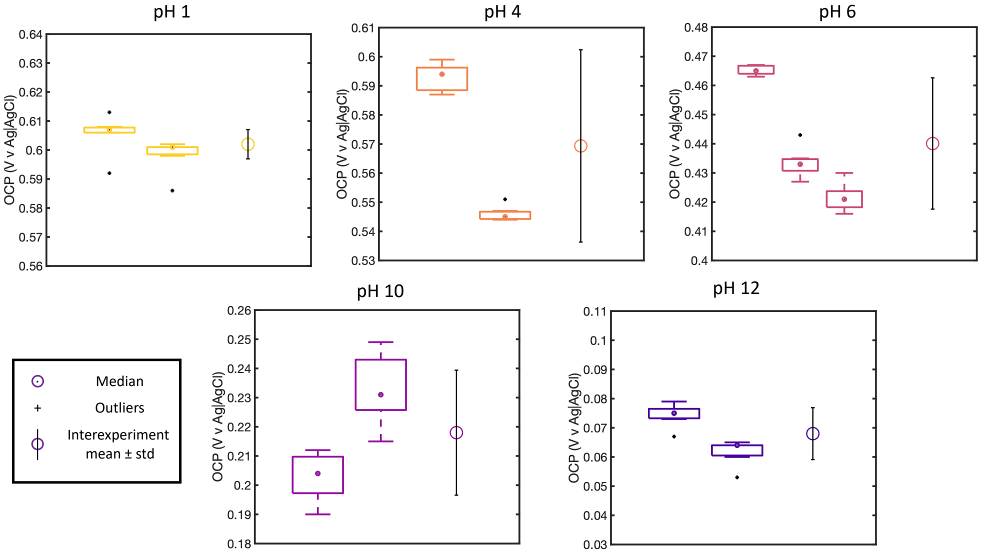

Figure 2.1: *Boxplots representing the variability of OCP within experiments for saline solutions of all pH (n = 7 for each boxplot). The error bars on the right hand side show the mean ± standard deviation of the average OCP of each experiment.*

Table 2.1: *Linear fit gradients of anodic and cathodic potentials vs pH for all k-values and 95% confidence intervals.*

k	**Gradient** E_{ano} (mV)	**95% CI**	**Gradient** E_{cat} (mV)	**95% CI**
0.566	-39.98	[-56.40 ; -23.56]	-40.61	[-53.75 ; -27.48]
1.25	-40.89	[-63.95 ; -17.83]	-34.79	[-51.28 ; -18.30]
1.55	-40.86	[-62.49 ; -19.23]	-27.43	[-47.81 ; -7.06]
1.66	-44.17	[-62.74 ; -25.60]	-29.52	[-49.46 ; -9.58]
1.75	-42.47	[-59.46 ; -25.47]	-30.27	[-47.88 ; -12.66]
1.85	-42.97	[-69.28 ; -16.66]	-29.84	[-52.71 ; -6.98]
2	-43.66	[-67.5 ; -19.10]	-29.38	[-43.69 ; -15.10]

Chapter 3

Appendix C

3.1 Additional COMSOL figures

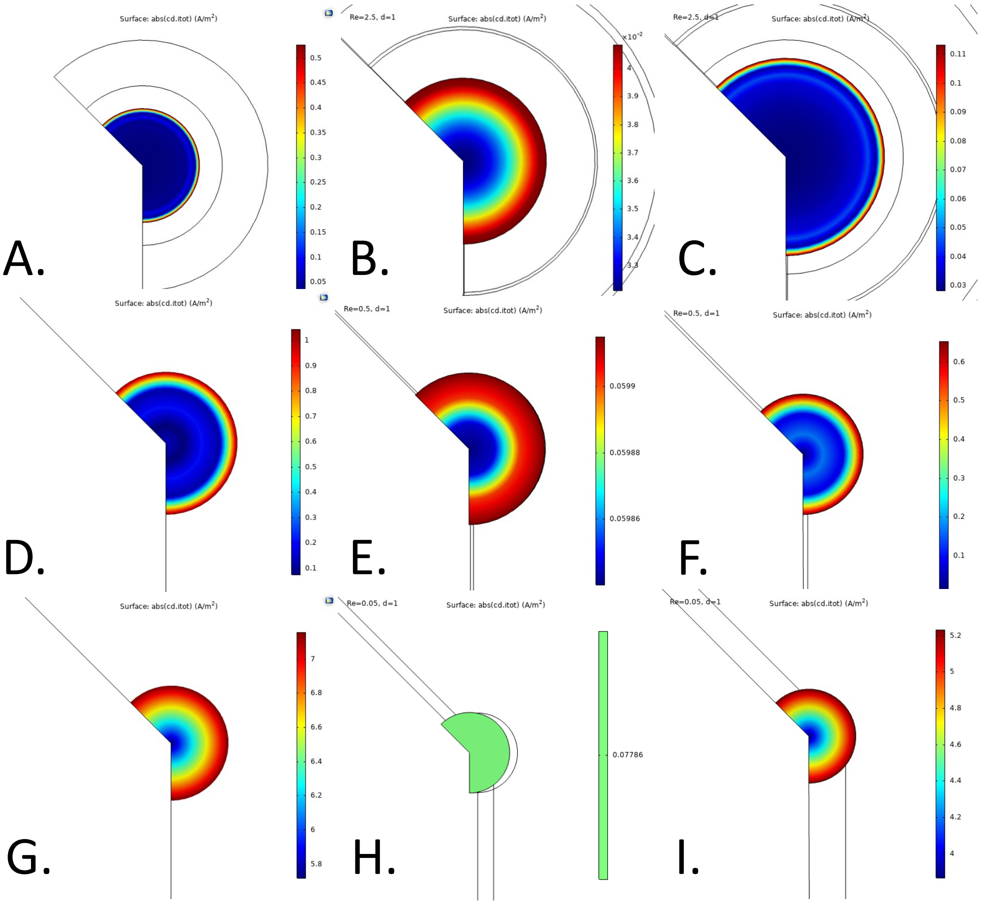

Figure 3.1: *Comparison of heatmaps for non-recessed (left column), tubular recess (center), and conical recess (right) at AR 0.2 (top row), AR 1 (middle), and AR 10 (right).*

Bibliography

A. J. Bard, L. R. Faulkner, and H. S. White. *Electrochemical methods: fundamentals and applications.* John Wiley & Sons, 2022.

A. R. Harris. Limitations in the electrochemical analysis of voltage transients. *Journal of Neural Engineering*, 21(1):013003, 2024.

D. W. Kumsa, F. W. Montague, E. M. Hudak, and J. T. Mortimer. Electron transfer processes occurring on platinum neural stimulating electrodes: pulsing experiments for cathodic-first/charge-balanced/biphasic pulses for $0.566 \leq$ k ≤ 2.3 in oxygenated and deoxygenated sulfuric acid. *Journal of neural engineering*, 13(5):056001, 2016.

D. W. Kumsa, N. Bhadra, E. M. Hudak, and J. T. Mortimer. Electron transfer processes occurring on platinum neural stimulating electrodes: pulsing experiments for cathodic-first, charge-balanced, biphasic pulses for $0.566leq$ kleq 2.3 in rat subcutaneous tissues. *Journal of neural engineering*, 14(5): 056003, 2017.